

On type I cascaded quadratic soliton compression in lithium niobate: Compressing femtosecond pulses from high-power fiber lasers

Morten Bache^{1,*} and Frank W. Wise²

¹*DTU Fotonik, Department of Photonics Engineering,
Technical University of Denmark, DK-2800 Kgs. Lyngby, Denmark*

²*Department of Applied and Engineering Physics, Cornell University, Ithaca, New York 14853*
(Dated: October 29, 2018)

The output pulses of a commercial high-power femtosecond fiber laser or amplifier are typically around 300-500 fs with a wavelength around 1030 nm and 10s of μJ pulse energy. Here we present a numerical study of cascaded quadratic soliton compression of such pulses in LiNbO_3 using a type I phase matching configuration. We find that because of competing cubic material nonlinearities compression can only occur in the nonstationary regime, where group-velocity mismatch induced Raman-like nonlocal effects prevent compression to below 100 fs. However, the strong group velocity dispersion implies that the pulses can achieve moderate compression to sub-130 fs duration in available crystal lengths. Most of the pulse energy is conserved because the compression is moderate. The effects of diffraction and spatial walk-off is addressed, and in particular the latter could become an issue when compressing in such long crystals (around 10 cm long). We finally show that the second harmonic contains a short pulse locked to the pump and a long multi-ps red-shifted detrimental component. The latter is caused by the nonlocal effects in the nonstationary regime, but because it is strongly red-shifted to a position that can be predicted, we show that it can be removed using a bandpass filter, leaving a sub-100 fs visible component at $\lambda = 515$ nm with excellent pulse quality.

PACS numbers: 42.65.Re, 42.65.Ky, 05.45.Yv, 42.70.Mp, 42.65.Hw, 42.65.Jx, 42.65.Jx

I. INTRODUCTION

Pulsed fiber laser systems are currently undergoing a rapid development, and by employing the chirped pulse amplification (CPA) technique high-energy femtosecond pulses can be generated with μJ -sub-mJ pulse energies [1]. Combined with the fact that the fiber laser technology offers a rugged, cheap and compact platform, ultrafast fiber CPA (fCPA) systems could compete with solid-state amplifier systems. However, the gain bandwidth of the Yb-doped fibers typically used for lasing in the 1.0 μm region is considerably lower than competing solid-state materials (such as Ti:Sapphire crystals). Thus, due to the build up of an excessive nonlinear phase shift Yb-based fCPA lasers are often limited to a pulse duration that typically is sub-ps at best (around 500 – 700 fs) for ~ 100 μJ pulses [2] while shorter pulses can be reached (~ 250 fs) for ~ 30 μJ pulses [3].

Efficient external compression methods are therefore needed. A prototypical compressor consists of a piece of nonlinear material, where a broadening of the pulse bandwidth occurs by self-phase modulation (SPM), followed by a dispersive element (gratings or chirped mirrors) that provides temporal compression. With this method (using a short piece of fiber as nonlinear material) 27 fs sub- μJ pulses were generated from 270 fs 0.8 μJ pulses from an fCPA system [4]. Alternative methods consist of using long (0.5 m or more) gas cells or filaments [5] as nonlinear material, and this works with pulse energies from

50 μJ to around 1 mJ (limited in part by self-focusing effects) or possibly even higher energies [6].

Using soliton compression both the SPM-induced pulse broadening and dispersion-induced compression occur in the same material [7]. However, as self-focusing solitons require anomalous dispersion this can only be achieved in the near-IR through strong waveguide dispersion. This means using specially designed fibers, such as micro-structured fibers. Fibers have a very limited maximum pulse energy of a few nJ, albeit large mode-area micro-structured solid-core and hollow-core fiber compressors can support up to 1 μJ [8].

Unfortunately the pulse energy from fCPA systems lies exactly in the gap between these methods. We will here study a compression method that can compensate for this. It is a soliton compressor based on cascaded quadratic nonlinearities [9–11], see Fig. 1. This has several advantages: As it relies on a self-defocusing nonlinearity, there are no problems with self-focusing effects, and multi-mJ pulse-energies can be compressed. Moreover, solitons require normal instead of anomalous dispersion, implying that solitons can be generated in the

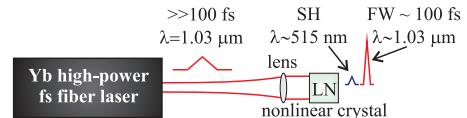


FIG. 1. (Color online) The cascaded quadratic soliton compressor studied here: the Yb fiber laser produces energetic longer pulses ($\gg 100$ fs) that are launched collimated in a quadratic nonlinear lithium niobate crystal, where the phase-mismatched type I SHG process compresses the input pulse.

*moba@fotonik.dtu.dk

visible and near-IR. Finally, it is extremely simple as it relies on just a small piece of quadratic nonlinear crystal, preceded only by a lens or a beam expander [12].

The basis for the cascaded quadratic soliton compressor (CQSC) is phase-mismatched second-harmonic generation (SHG). The cascaded energy transfer from the pump (fundamental wave, FW) to the second harmonic (SH) and back imposes a strong SPM-like nonlinear phase shift on the FW, whose sign can be made self-defocusing [13, 14]. Thereby the FW pulse can be compressed with normal dispersion [9], and soliton compression becomes possible in the visible and near-IR [10].

In this paper we investigate the CQSC in a type I lithium niobate (LiNbO_3 , LN) crystal, where the goal is to perform moderate compression of longer fs pulses from fCPA systems at the Yb gain wavelength of 1030 nm. We show that in order to overcome the detrimental cubic nonlinearities the phase mismatch has to be chosen so low so that the compression occurs in the so-called nonstationary regime. This regime is dominated by group-velocity mismatch (GVM) effects, and exactly the large GVM is a well-known drawback of using LN in the near-IR for SHG. However, when only moderate compression is desired, the soliton order can be kept low, and we show through numerical simulations that reasonable pulse quality can be achieved and that up to 80% of the pulse energy is retained in the central spike. The compression limit is found to be around 120 fs FWHM, which is a limit set by the GVM effects. The compression occurs in a crystal of reasonable length, 10 cm. This is possible only because LN has a very large 2. order dispersion. Finally, we show that bandpass filtering of the SH actually can lead to a very clean sub-100 fs visible pulse with around 0.1% conversion efficiency.

In this paper we first discuss the general compression properties of LN in a cascaded type I SHG interaction setup in Sec. II, and then show some numerical simulations in Sec. III of pulses coming from two different commercially available fCPA systems. We conclude in Sec. IV. The properties of LN are discussed in App. A, and App. B discusses the anisotropic Kerr nonlinear response of LN. Appendix C and D discuss the conversion relations between Gaussian and SI units for cubic nonlinear coefficients and Miller's rule, respectively.

II. TYPE I COMPRESSION PROPERTIES OF LITHIUM NIOBATE CRYSTALS

With the CQSC high-energy few-cycle compressed pulses can be generated, as was experimentally observed at 1250 nm [15]. However, the first studies performed at 800 nm were plagued by GVM effects, that prevented reaching the few-cycle regime [9, 10, 15]. These studies used a β -barium-borate (BBO) crystal in a type I SHG $oo \rightarrow e$ configuration, where the FW (ordinary polarization) is orthogonal to the SH (extraordinary polarization) and where birefringent phase matching is possible

by angle-tuning the crystal. BBO is in many respects an ideal nonlinear crystal: it has low dispersion, a very large transparency window, and a reasonably strong quadratic nonlinearity relative to the detrimental cubic one. As we have shown in previous theoretical and numerical studies, BBO provides an excellent compression of longer pulses to ultra-short duration at the Yb gain wavelengths [16–18]. The problem with BBO is that good quality waveguides are not supported and that it is very difficult to grow long crystals. Especially the latter is important if only moderate compression of longer pulses is desired. In moderate soliton compression most of the pulse energy is conserved in the compressed pulse, and the pulse has a reduced pedestal. The problem is that compression will only occur after a long propagation length.

We therefore turn here to LN, which is a widely used quadratic nonlinear crystal for IR frequency conversion. LN is attractive due to extremely large effective quadratic nonlinearities (up to 10 times larger than BBO), that can be accessed through a quasi-phase matched (QPM) type 0 SHG phase matching configuration where FW and SH have identical polarization. However, here we study LN in a type I configuration as BBO. The effective quadratic nonlinearity is more than twice as large as in BBO.

LN is usually not considered very suitable for SHG of short pulses in the near-IR because the SH becomes very dispersive; thus, the FW and SH group velocities are very different resulting in large GVM. This is also why LN has not been used in the near-IR as nonlinear medium for the CQSC, for which GVM is a very detrimental effect. Another disadvantage for the CQSC is that the Kerr nonlinear response is several times larger than BBO, which counteracts the advantage of the large quadratic nonlinearity of LN. Therefore the CQSC experiments done so far using LN were done in the telecommunication band and exploited QPM in a type 0 configuration [19], where effective quadratic nonlinearity is around three times larger than what can be achieved in a type I configuration. However, we now show that type I LN offers a quite decent compression performance without having to custom design a QPM grating.

A. Solitons with cascaded quadratic nonlinearities

In cascaded quadratic interaction the FW effectively experiences a Kerr-like nonlinear refractive index. This is in addition to the cubic (Kerr) nonlinearities that are always present in all media. We can write the total refractive index of the FW [see Eq. (C2)]

$$n = n_1 + \frac{1}{2}|\mathcal{E}_1|^2 n_{\text{cubic}} = n_1 + I_1 n_{\text{cubic}}^I \quad (1)$$

where n_1 is the FW linear refractive index, \mathcal{E}_1 is the FW electric field, and I_1 the FW intensity. It is typical to report the nonlinear refractive index relative to the electric field, n_{cubic} , or to the intensity, n_{cubic}^I . We have here for simplicity neglected cross-phase modulation (XPM) contributions since they are small in cas-

caded SHG. As mentioned we have contributions from both cascaded quadratic and cubic Kerr nonlinearities

$$n_{\text{cubic}}^I = n_{\text{SHG}}^I + n_{\text{Kerr},11}^I \quad (2)$$

where $n_{\text{Kerr},11}^I$ is the SPM Kerr nonlinear refractive index of the FW (see App. B for details on the notation etc.). The contribution from the cascaded quadratic nonlinearities can in the large phase mismatch limit ($\Delta k L \gg 1$, where L is the crystal length) be approximated as [13]

$$n_{\text{SHG}}^I \simeq -\frac{4\pi d_{\text{eff}}^2}{c\epsilon_0\lambda_1 n_1^2 n_2 \Delta k} \quad (3)$$

where d_{eff} is the effective $\chi^{(2)}$ nonlinearity. For $\Delta k = k_2 - 2k_1 > 0$ the cascaded contribution is negative, i.e. self-defocusing. Here $k_j = 2\pi/\lambda_j$ is the wavenumber.

The effective quadratic nonlinearity of the type I $oo \rightarrow e$ interaction for the $3m$ crystal class (LN, BBO) is

$$d_{\text{eff}} = d_{31} \sin \theta - d_{22} \cos \theta \sin 3\phi \quad (4)$$

where the angles are defined in Fig. 9 in App. B. Choosing $\phi = -\pi/2$ gives maximum nonlinearity (see App. A).

In cascaded quadratic soliton compression the aim is to get $n_{\text{SHG}}^I < 0$ and $|n_{\text{SHG}}^I| > n_{\text{Kerr},11}^I$ as to achieve a total self-defocusing cubic nonlinearity. The soliton interaction can then be described by an effective soliton order [17]

$$\begin{aligned} N_{\text{eff}}^2 &= N_{\text{SHG}}^2 - N_{\text{Kerr}}^2 \\ &= L_{D,1} k_1 I_{\text{in}} (|n_{\text{SHG}}^I| - n_{\text{Kerr},11}^I) \end{aligned} \quad (5)$$

where $N_{\text{SHG}} = L_{D,1} k_1 I_{\text{in}} |n_{\text{SHG}}^I|$ is the soliton order of the self-defocusing cascaded quadratic nonlinearity, and $N_{\text{Kerr}} = L_{D,1} k_1 I_{\text{in}} n_{\text{Kerr},11}^I$ is the soliton order of the material Kerr self-focusing cubic nonlinearity. The FW dispersion length is $L_{D,1} = T_{\text{in}}^2/|k_1^{(2)}|$, where $k_1^{(2)}$ is the FW group-velocity dispersion (GVD). We generally use the following notation for the dispersion parameters $k_j^{(m)} = \partial^m k_j / \partial \omega^m |_{\omega=\omega_j}$.

B. Linear and nonlinear response of LN at 1.03 μm

Selecting $\lambda_1 = 1.03 \mu\text{m}$, the operating wavelength of most Yb-based fiber laser amplifiers, the properties of LN are summarized in Fig. 2: the phase mismatch (a) becomes small at $\theta \simeq 1.3$ radians ($70 - 75^\circ$). As shown in (e) in this range $d_{\text{eff}} \simeq 5.2 \text{ pm/V}$, and the total nonlinear refractive index (f), as expressed by Eq. (2), can become negative, implying that the cascaded nonlinearity is stronger than the Kerr nonlinearity. This happens for $\Delta k < 62 \text{ mm}^{-1}$ (or $\theta > 70.4^\circ$). At $\theta = 75.8^\circ$ phase matching is achieved, after which $n_{\text{SHG}}^I > 0$ and thus self-focusing.

GVM is very large, see Fig. 2(b), which as we will see later sets a strong limitation to the compression performance. The GVD is shown in Fig. 2(c), and importantly FW GVD (red) is large and normal (i.e. positive). It will stay normal until $\lambda_1 > 1.9 \mu\text{m}$, after which it becomes

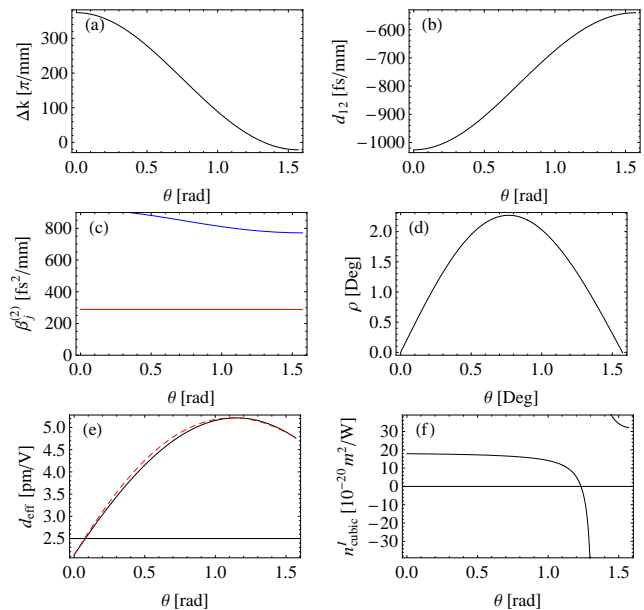


FIG. 2. (Color online) Properties at $\lambda_1 = 1.03 \mu\text{m}$ when angle-tuning the LN crystal: (a) Phase mismatch, (b) GVM parameter, (c) GVD of FW (red) and SH (blue), and (d) the spatial walk-off angle ρ . The effective quadratic nonlinearity neglecting (black) and including (dashed red) spatial walk-off are shown in (e) and (f) is the total cubic Kerr nonlinearity (2) from cascaded quadratic nonlinearities and Kerr SPM (using $n_{\text{Kerr}}^I = 18 \times 10^{-20} \text{ m}^2/\text{W}$, see App. B).

anomalous and self-defocusing solitons are no longer supported. The SH GVD (blue) is about 3 times larger than the FW GVD.

Since the type I critical phase matching is employed, the walk-off angle $\rho = \arctan[\tan(\theta)n_o^2/n_e^2] - \theta$ (valid for a negative uniaxial crystal) is nonzero, see Fig. 2(d). In Fig. 2(e) it is apparent that d_{eff} is largely unaffected by walk-off. However, walk-off does set a limit to the effective interaction length between the pump and the SH as we will discuss later.

C. Compression diagram for type I LN

We now generalize to other wavelengths and summarize the type I compression performance of LN in Fig. 3¹. This compression diagram shows the different compression regimes for the CQSC as the wavelength and the phase mismatch is varied.

Above the red curve the total nonlinear refractive index is focusing $n_{\text{cubic}}^I > 0$, so solitons are not supported since

¹ The specific crystal chosen in this work is 1% MgO doped stoichiometric LN, as the MgO doping gives a much higher material damage threshold. Also 5% MgO doped congruent LN would work well. See App. A for more details about the crystal.

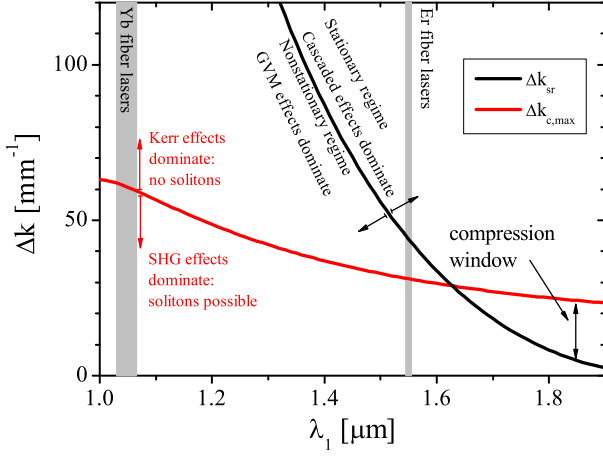


FIG. 3. (Color online) Compression diagram for 1% MgO:sLN at room temperature and aligned for type I SHG. For various pump wavelengths λ_1 the choice of phase-mismatch parameter Δk affects the compression. In order to excite solitons the phase-mismatch must be kept below the red line ($\Delta k < \Delta k_{c,\max}$), because otherwise the material cubic nonlinearities are too strong ($n_{\text{Kerr},11}^I > |n_{\text{SHG}}^I|$). Optimal compression occurs when the cascaded nonlinearities dominate over GVM effects ($\Delta k > \Delta k_{\text{sr}}$, above the black line). We have also indicated the operation wavelengths of Yb and Er doped fiber lasers. The red line uses Miller’s rule to estimate the nonlinear quadratic and cubic susceptibilities at other wavelengths, cf. Eqs. (D1)-(D2), and uses $n_{\text{Kerr},11}^I = 20 \times 10^{-20} \text{ m}^2/\text{W}$ for $\lambda = 0.78 \text{ } \mu\text{m}$ (see App. B for an extended discussion).

the FW GVD is normal. The curve is found by setting $|n_{\text{SHG}}^I| = n_{\text{Kerr},11}^I$ giving [17]

$$\Delta k_{c,\max} = k_1 \frac{2d_{\text{eff}}^2}{c\epsilon_0 n_1^2 n_2 n_{\text{Kerr},11}^I} \quad (6)$$

Below the black curve the compression performance is dominated by GVM effects (nonstationary regime) while above it is dominated by cascaded effects (stationary regime). The curve is to second order ² given by [16]

$$\Delta k_{\text{sr}} = \frac{d_{12}^2}{2k_2^{(2)}} \quad (7)$$

where $d_{12} = k_1^{(1)} - k_2^{(1)}$ is the GVM parameter and $k_2^{(2)}$ is the SH GVD. The lower this curve is the better because this implies that the chance of observing solitons in the stationary regime increases. Thus, the very large GVM parameter d_{12} is detrimental because it pushes the curve upwards. Instead the huge SH GVD values, see Fig. 2 (c), are actually helping to push the curve downwards. Therefore a large SH GVD can actually be beneficial for clean soliton compression.

² A more accurate transition can easily be calculated numerically using the full SH dispersion operator [18], which we have done in what follows.

The optimal compression occurs in the so-called “compression window” [16], where the soliton compressor works most efficiently because solitons are supported in the stationary regime. The diagram shows a compression window for type I LN in the regime $\lambda_1 = 1.6 - 1.9 \text{ } \mu\text{m}$. Unfortunately in this range there are no fCPA systems.

Fortunately, as we will show also in the nonstationary regime compression is possible, as long as the effective soliton order is low enough. This is what we will try to exploit in the regime around $\lambda_1 \sim 1.03 - 1.06 \text{ } \mu\text{m}$.

Coming back to $\lambda_1 = 1.03 \text{ } \mu\text{m}$ we observe that solitons are supported for when $0 \ll \Delta k < \Delta k_{c,\max} = 62 \text{ mm}^{-1}$. However, when getting too close to $\Delta k_{c,\max}$ the intensities required to observe solitons become very large implying excessive Kerr XPM effects and increased Raman-like GVM effects [18]. On the other hand for Δk too small the cascading limit ceases to hold, and also the compressor performance decreases due to excessive GVM effects [18]. In fact, as a rule of thumb the compression limit in the nonstationary regime (in which the system will always be for $\Delta k \sim 0$) the compression limit is roughly given by the pulse duration for which $L_{\text{coh}} = L_{\text{GVM}}$, where $L_{\text{coh}} = \pi/|\Delta k|$ is the coherence length and $L_{\text{GVM}} = \Delta t_{\text{soliton}}/|d_{12}|$ is the *dynamic* GVM length of a sech-shaped soliton. With “dynamic” we mean that the GVM length changes as the soliton compresses. Thus, in the nonstationary regime the limit is ³

$$\Delta t_{\text{limit}}^{\text{FWHM}} \sim 2 \ln(1 + \sqrt{2}) \frac{\pi |d_{12}|}{|\Delta k|} \quad (8)$$

where the factor in front of the fraction is the conversion factor to FWHM for a sech-shaped pulse. Obviously as Δk approaches the phase matching point the soliton cannot compress to short durations. We numerically found the optimal compression point in the $\Delta k = 35 - 50 \text{ mm}^{-1}$ regime, and with the best results for $\Delta k = 45 \text{ mm}^{-1}$, for which $n_{\text{SHG}}^I = 25 \times 10^{-20} \text{ m}^2/\text{W}$.

D. Predicting the compression performance

The next step is to estimate what the compression performance could look like. Here the scaling laws ⁴ come into the picture, which can be used to predict the propagation distance for optimal compression z_{opt} , the compression factor f_c and the pulse quality Q_c [17].

As we have pointed recently [16], it is the phase mismatch and the GVM (zero and first order dispersion) that really control the compression properties. The only requirement to the second order dispersion is that FW

³ Note that this expression differs with a factor of $\pi/2$ from the limit $T_{R,\text{SHG}} = 2|d_{12}/\Delta k|$ that we suggested in [18]; this is purely an empirical choice.

⁴ Note that the scaling laws presented here are only ball-park figures when used in the nonstationary regime as they were found in the stationary regime.

GVD is normal $k_1^{(2)} > 0$ as to support solitons. Otherwise as we discuss below the FW GVD is basically just determining the optimum compression length. The SH GVD instead plays a minor role in the compression properties, cf. Eq. (7). Our initial idea was to exploit that LN is quite dispersive when pumped at $\lambda_1 \sim 1.0 \mu\text{m}$, so the very large FW GVD makes it possible to compress the pulse in a short crystal.

So why and when is it interesting to increase GVD as to compress in a short crystal? Obviously, the crystals have length limits, which for LN is around 100 mm. The optimal compression point scales as [17]

$$\frac{z_{\text{opt}}}{z_0} = \frac{0.44}{N_{\text{eff}}} + \frac{2.56}{N_{\text{eff}}^3} - 0.002. \quad (9)$$

where $z_0 = \frac{\pi}{2}L_{D,1}$ is the soliton length [20]. So the point where the pulse compression is optimal depends on the effective soliton order, the input pulse duration and the FW GVD. Therefore since quality LN crystals are maximum 100 mm long, the CQSC works best when the soliton order is large and the GVD length is short. But when the soliton order is large, the detrimental effects due to GVM are strongly increased [15, 18], in particular in the nonstationary regime. Therefore, in the case we study here clean compression can only be done with low soliton order, and therefore the FW GVD must be large as to ensure compression in realistic crystal lengths.

A downside to the large GVD is the following: given that some effective soliton order is required then since $N_{\text{eff}} \propto \sqrt{I_{\text{in}}L_{D,1}} \propto T_{\text{in}}\sqrt{I_{\text{in}}/|k_1^{(2)}|}$ we have that a large GVD gives a short GVD length, and thus larger intensities are needed to excite a soliton. The same problem is found for short input pulses, say from a Ti:Sapphire amplifier. However, this is only an issue if operating with intensities close to the damage threshold, which is not the case here: the intensities are moderate ($I_{\text{in}} \ll 100 \text{ GW/cm}^2$), and instead our issue is to get the solitons to compress in a crystal that is not too long.

The compression factor $f_c = T_{\text{in}}/\Delta t_{\text{opt}}$, where Δt_{opt} is the pulse compressed pulse duration at z_{opt} , is also affected by the effective soliton order [17]

$$f_c = 4.7(N_{\text{eff}} - 0.86) \quad (10)$$

The pulse quality can also be predicted, and is defined as the ratio between the compressed pulse fluence with that of the input pulse. It scales as [17]

$$Q_c = [0.24(N_{\text{eff}} - 1)^{1.11} + 1]^{-1}. \quad (11)$$

We can use this to calculate the compressed pulse peak intensity $I_{\text{opt}} = Q_c f_c I_{\text{in}}$ and energy $E_{\text{opt}} = Q_c E_{\text{in}}$. An advantage of using low soliton orders is that Q_c remains high, and thus the compressed pulse retains most of the initial pulse energy.

E. Compression performance of fCPA systems

Let us use these scaling laws to predict the compression performance of fCPA systems. High-energy femtosecond pulses from fCPA systems use both Yb doped and Er doped gain fibers. Since fCPA systems are diode pumped with a wavelength just below $1.0 \mu\text{m}$ the quantum efficiency of Yb doped systems is higher, and therefore the majority of commercial and scientific systems prefer to use Yb over Er. Most systems operate at the $\lambda = 1.03 \mu\text{m}$ Yb emission line and can for low pulse energies ($< 15 \mu\text{J}$) generate pulses as short as 250 fs, while higher pulse energies result in longer pulses (currently $50 \mu\text{J}$ 450 fs pulses is the state-of-the-art for commercial systems). In Er amplifier systems much lower pulse energies are available, typically $1 - 3 \mu\text{J}$ and 500 - 700 fs pulses at $\lambda = 1.55 \mu\text{m}$; such low pulse energies and long pulse duration mean that only very low soliton orders can be excited, and thus the CQSC can only achieve very moderate compression occurring in very long crystals.

The basis for the following case studies and numerical simulations is therefore a couple of commercially available Yb-based fCPA systems, both operating at 1030 nm. Case (1) is a Clark MXR Impulse⁵ giving $15 \mu\text{J}$ 250 fs FWHM pulses, which represents a system giving quite short, yet still reasonably energetic pulses as a starting point. Case (2) is an Amplitude Systemes Tangerine⁶ giving $50 \mu\text{J}$ 450 fs FWHM pulses, which represents a system with more energetic but also longer pulses.

The two cases are studied together taking $\Delta k = 45 \text{ mm}^{-1}$. Figure 4(a) shows that in case (1) we need to focus the pulses to $w_0 < 600 \mu\text{m}$ to observe solitons: in this regime Fig. 4(d) shows that the Rayleigh length $z_R = \pi w_0^2/\lambda$ is only 5-6 times larger than the optimal compression point z_{opt} of around 100 mm. This is borderline at the risk of experiencing diffraction problems. Even increasing or decreasing the waist does not improve this ratio much. In case (2) instead, the increased pulse energy makes solitons appear already at $w_0 \simeq 1.6 \text{ mm}$, despite the longer pulse duration. This means that diffraction should be less of an issue: in Fig. 4(d) the pulse compression point relative to the Rayleigh length of the focused beam is significantly smaller in case (2).

Fig. 4(c) indicates that the spatial walk-off in the crystal can become an issue: the crystal should be shorter than the spatial walk-off length $L_{\text{wo}} = w_0/\tan \rho \simeq w_0/\rho$ to ensure proper interaction between the FW and the SH, but evidently the pulse compression lengths in both cases are at least a factor of 2-3 longer than the spatial walk-off length. It might therefore be necessary to compensate for this by using two crystals, one inverted relative to the other so the walk-off direction in the 2. crystal is inverted with respect to the 1. crystal [21].

⁵ <http://www.clark-mxr.com>

⁶ <http://www.amplitude-systemes.com>

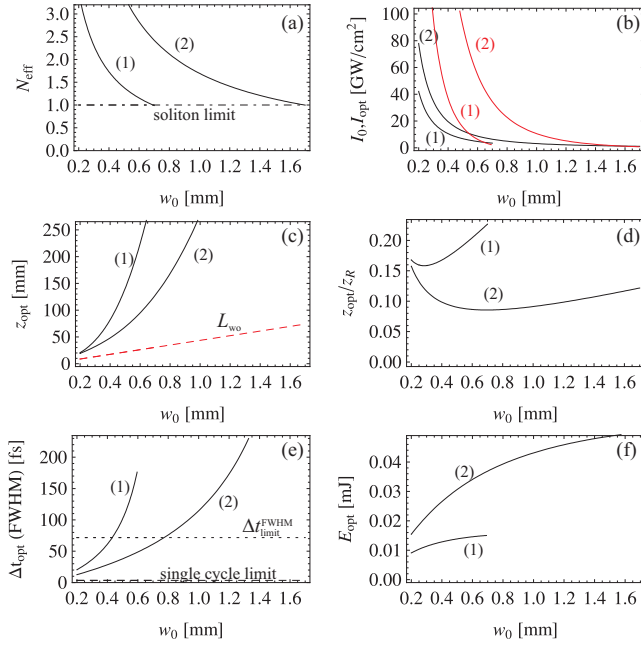


FIG. 4. (Color online) Practical operation range of the LN type I compression system at $\lambda_1 = 1.03 \mu\text{m}$ for $\Delta k = 45 \text{ mm}^{-1}$. The plots show the predicted behaviour when the FW waist w_0 is varied. The two cases are (1) pump pulses with $T_{\text{in}}^{\text{FWHM}} = 250 \text{ fs}$ and $15 \mu\text{J}$ pulse energy, and (2) pump pulses with $T_{\text{in}}^{\text{FWHM}} = 450 \text{ fs}$ and $50 \mu\text{J}$ pulse energy. The curves in (b)-(f) are calculated based on N_{eff} shown in (a) by using the scaling laws [17] that hold for $N_{\text{eff}} > 1$.

An alternative solution to the walk-off problem is to turn to a noncritical phase matching scheme, where $\rho = 0$. This happens for $\theta = 0$ or $\pi/2$, see Fig. 2(d). Of course this removes the possibility of tuning the phase matching via θ , and one has to turn to temperature tuning of Δk . The temperature needed to get to the desired operation point ($\Delta k \simeq 40 - 50 \text{ mm}^{-1}$) can be estimated using the temperature dependent Sellmeier equations [22], and our calculations indicate that it should happen already at a temperature of around 45° C . This would make an easy solution to the walk-off problem.

The strong GVM implies that compression of Yb-based systems can only occur in the nonstationary regime, see Fig. 3. Thus, unless N_{eff} is close to unity the GVM induced Raman-like effects dominate, and the FW pulse becomes extremely distorted and very poorly compressed. Actually, as a rule of thumb it never makes sense to use N_{eff} larger than what is sufficient to reach the limit expressed by Eq. (8), and typically even a N_{eff} smaller than that. The limit is drawn as a dotted line in Fig. 4(e), and it is reached around $w_0 = 400 \mu\text{m}$ in case (1) and $w_0 = 800 \mu\text{m}$ in case 2.

Finally, Fig. 4(b) shows that quite moderate input intensities must be used to achieve solitons in both cases. This is related to the quite long input pulse durations. Furthermore, Fig. 4(f) shows that the low soliton orders conserve most of the pulse energy in both cases.

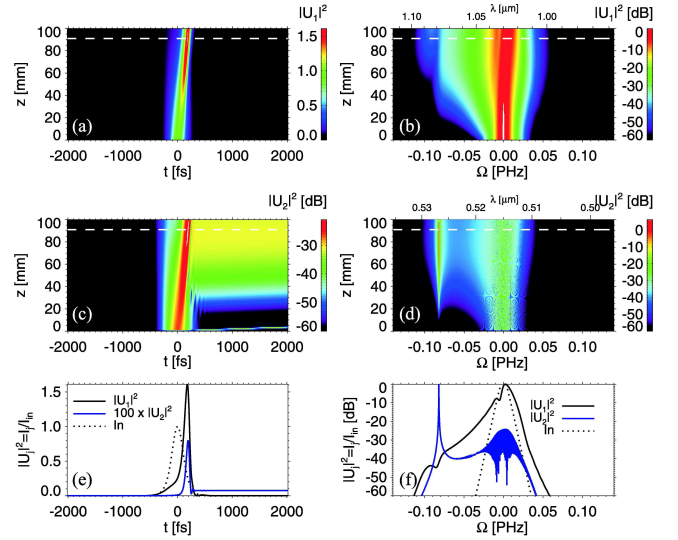


FIG. 5. (Color online) Numerical simulation of soliton compression in LN with $\lambda_1 = 1.03 \mu\text{m}$, $T_{\text{in}}^{\text{FWHM}} = 250 \text{ fs}$, $\Delta k = 45 \text{ mm}^{-1}$ and $N_{\text{eff}} = 1.4$ (implying $I_{\text{in}} = 6.9 \text{ GW/cm}^2$). The FW pulse shown in (a) compresses to $\Delta t_{\text{opt}} = 126 \text{ fs}$ (FWHM) after propagating 91 mm . The SH time plot (c) and FW (b) and SH (d) spectra are also shown on a logarithmic scale, and U_j are normalized to the peak input FW electric field. In (e) and (f) cuts are shown at the optimal compression point $z = 91 \text{ mm}$ (corresponding to the white line in the 2D plots). Note that the SH in (e) is magnified 100 times.

III. NUMERICAL SIMULATIONS

We here present numerical simulations of the two cases using a plane-wave temporal model based on the slowly evolving wave equation (see more details in [17] and references therein), which includes self-steepening effects and higher-order dispersion. This model is justified as long as diffraction is minimal, which we assume is the case when the crystal length is much shorter than the Rayleigh length, and when spatial walk-off is minimal. This requirement will be discussed further below.

A. Case (1): 250 fs 15 μJ pulses

For the 250 fs $15 \mu\text{J}$ pulses from a Clark laser system we found that the best compression was obtained with $N_{\text{eff}} \sim 1.3 - 1.5$. This soliton order can be achieved with $15 \mu\text{J}$ pulse energy when the pump is focused to around $w_0 = 400 \mu\text{m}$, see Fig. 4(a).

The theoretical compression factor for such soliton orders is $f_c = 2 - 3$, *i.e.*, a $\Delta t_{\text{opt}} \sim 80 - 125 \text{ fs}$ FWHM compressed pulse is predicted. In Fig. 5 we show the results of a simulation with $N_{\text{eff}} = 1.4$. This soliton order gave the best compression: a slightly asymmetric $\Delta t_{\text{opt}} = 126 \text{ fs}$ (FWHM) pulse is observed after 91 mm of propagation, see (a) and cut in (e). The compression is not quite as strong as predicted by the scaling law (10), but this is

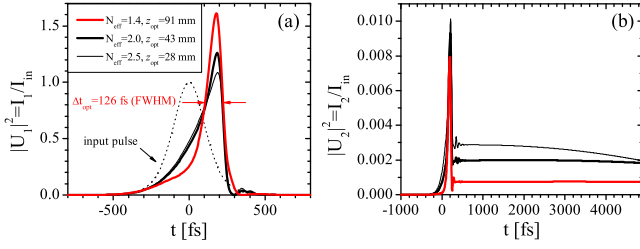


FIG. 6. (Color online) Simulations as in Fig. 5 but with increasing N_{eff} . The red curve corresponds to the optimal compression point from Fig. 5(e), while the black curves show what happens as the effective soliton order increases (making the optimal compression point occurring sooner).

because the scaling laws are based on pulse compression in the stationary regime. On the other hand the pulse quality is large, $Q_c = 0.82$, so most of the pulse energy is retained in the central compressed part, and the pulse pedestal is also very small. These are the main advantages of soliton compression with low soliton orders.

The FW spectrum (b) experiences upon propagation SPM-like broadening, where the blue-shifted shoulder clearly dominates; this is a sign of the cascaded quadratic nonlinearities dominating, and the fact that it is blue shifted is related to the negative sign of d_{12} .

In the SH time-plot (c) we observe the strong GVM first inducing a weak component quickly escaping from the central part of the pulse, and later the GVM induces the characteristic DC-like trailing temporal pulse in the SH (this often occurs close to or at phase matching in presence of GVM, see also [23]). This behaviour is also reflected in the SH spectrum, see (d) and cut in (f), which shows a very strong and extremely narrow red-shifted component building up, which eventually becomes the dominating contribution. As we discuss below its spectral position can accurately be predicted by the nonlocal theory that was recently developed by us [16, 18]. We believe that this strong and long SH trailing component actually causes the trailing part of the FW to be strongly depleted, and that this is the main reason for the asymmetrical FW shape.

The question is now: can we increase the effective soliton order and achieve further compression below 100 fs as to approach the limit predicted by Eq. (8)? This turns out to be impossible: when N_{eff} is increased the GVM effects become stronger, making the compressed pulse more distorted. This is clearly observed in Fig. 6, where we increase N_{eff} and compare with the compression of Fig. 5: For $N_{\text{eff}} = 2.0$ the compressed FW pulse in (a) is still quite short, but clearly is less clean. For $N_{\text{eff}} = 2.5$ the compressed pulse instead becomes quite distorted. It is also evident in the SH time plots that the trailing DC-like component increases with N_{eff} , while the central part in all cases is a sub-100 fs FWHM pulse. It is quite weak because most of the converted SH energy is fed into the DC-like part of the pulse, which is connected to the strong spectral peak in the SH spectrum. This spectral

peak becomes stronger with increased N_{eff} (not shown), but does not change position as it does not depend on N_{eff} .

In order to understand the spectral content of the different temporal components, the cross-correlation frequency-resolved optical gating (XFROG) method is useful. The spectral strength is given by [24]

$$S_j(z, T, \Omega) = \left| \int_{-\infty}^{\infty} dt e^{i\Omega t} \mathcal{E}_j(z, t) \mathcal{E}_{\text{gate}}(t - T) \right|^2 \quad (12)$$

where $\mathcal{E}_{\text{gate}}(t)$ is a properly chosen gating pulse. The spectrograms of the compressed pulses in Fig. 6 for $N_{\text{eff}} = 1.4$ are shown in Fig. 7. The FW compressed pulse is slightly blue-shifted (around 2 THz), and the compressed part (located at $T \sim 200$ fs) shows a significantly broader spectrum.

The SH spectrum is very particular: the part of the pulse that propagates with the FW group velocity (the “locked” part) shows a quite clean short pulse. This group velocity locking of the SH has been observed before [19, 23] and can be understood from the nonlocal theory [16, 18]: the SH has a component that is basically slaved to the FW due to the cascading nonlinearities. In frequency domain it can be compactly expressed as [18]

$$U_2(z, \Omega) \propto \tilde{R}_-(\Omega) \mathcal{F}[U_1^2(z, t)] \quad (13)$$

where $\mathcal{F}[\cdot]$ denotes the forward Fourier transform, and U_j are properly normalized fields. Thus, the spectral content of the SH is slaved to the spectral content of the spectrum of U_1^2 . The weight is provided by the nonlocal Raman-like response function in the nonstationary regime [18]

$$\tilde{R}_-(\Omega) = (2\pi)^{-1/2} \frac{\Omega_+ \Omega_-}{(\Omega - \Omega_-)(\Omega - \Omega_+)} \quad (14)$$

where $\Omega_{\pm} = \Omega_a \pm \Omega_b$. These frequencies can be calculated (to 2. order) from the dispersion of the system as $\Omega_a = d_{12}/k_2^{(2)} = -1.044$ PHz and $\Omega_b = |2\Delta k/k_2^{(2)} - \Omega_a^2|^{1/2} = 0.963$ PHz. In the center around $\Omega = 0$, where $\mathcal{F}[U_1^2(z, t)]$ is residing in this case, the response is quite flat: thus we get a SH component locked to the FW and when the FW compresses so does this SH component.

Another striking feature of the SH spectrogram is the DC-like component: it is very evident as a long pulse centered around $\Omega \sim -80$ THz. Also this peak can be understood from Eq. (13), because according to Eq. (14) the nonlocal response function in the nonstationary regime has sharp resonance peaks in the response at $\Omega = \Omega_{\pm}$. Inserting the dispersion values of the simulation we get $\Omega_+ = -81.6$ THz in excellent correspondence with the observed peak position as the red dashed line indicates. Instead Ω_- is located too far into the red side of the spectrum to affect the behaviour.

Considering this spectral composition, it might even be possible to filter away the disturbing SH component at $\Omega = \Omega_+$, which in time-domain would give a quite decent SH pulse. In (c) we show that this is feasible: we pass the SH pulse through a super-Gaussian ($n = 3$) bandpass

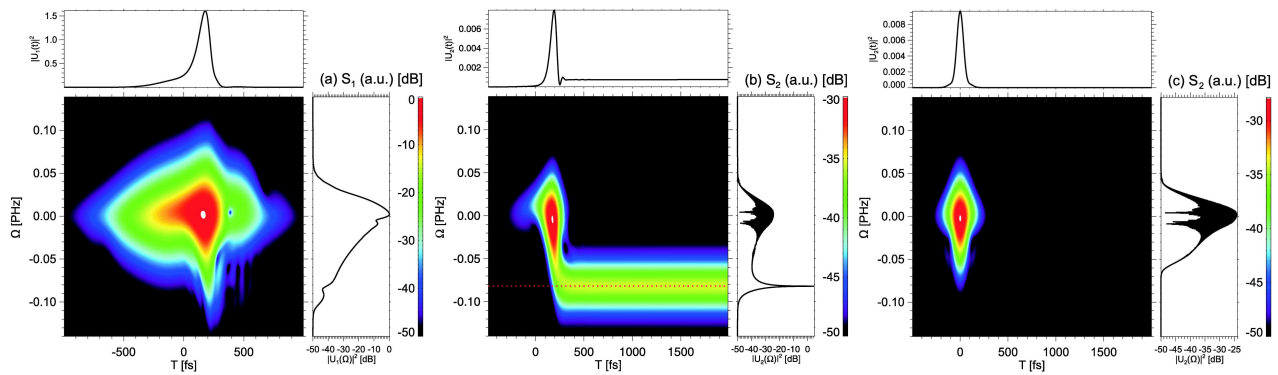


FIG. 7. (Color online) XFROG-like spectrograms of the simulation in Fig. 5 at the optimal compression point $z_{\text{opt}} = 91$ mm. The sech-shaped gating pulse had $T_0^{\text{FWHM}} = 70$ fs, and the spectrograms are normalized to the peak value of S_1 . The top and side plots show the purely temporal and spectral traces, respectively, and are thus identical to Fig. 5(e) and (f). The red dashed line in (b) indicates the value Ω_+ as calculated by the nonlocal theory. The spectrogram in (c) shows the SH passed through a 3. order super-Gaussian bandpass filter centered at the SH carrier frequency $\lambda_2 = 0.515$ μm and with a FWHM of 100 THz.

filter centered at ω_2 and with a bandwidth of 100 THz FWHM (corresponding to 15 nm): this filters away the disturbing sharp peak, and a 80 fs FWHM pulse remains at $\lambda = 0.515$ nm. The peak intensity in this short pulse is around $0.006I_{\text{in}} = 0.0414$ GW/cm². If we assume that it is created with 15 μJ pulse energy focused to $w_0 = 0.5$ mm to achieve $N_{\text{eff}} = 1.4$, and that the generated SH has roughly the same spot size, then the pulse energy of the filtered 80 fs pulse would be around 50 nJ.

B. Case (2): 450 fs 50 μJ pulses

In case (2) the pulse duration is longer, 450 fs. When the pulse duration is longer the soliton will for a fixed soliton order compress after a longer distance. This is because according to Eq. (9) $z_{\text{opt}} \propto L_{\text{D},1} \propto T_{\text{in}}^2$. However, we may compensate for this by increasing the effective soliton order enough to reach the limit governed by Eq. (8). For a 450 fs 50 μJ pulse it is achieved around $w_0 = 0.8$ mm, see Fig. 4(e), resulting in $N_{\text{eff}} \sim 2.0 - 2.5$. This higher soliton order should make it possible to com-

press in crystal lengths of around 10-15 cm, see Fig. 4(c).

In Fig. 8 we show some numerical simulations using these longer more energetic pulses. The best pulse observed shows a three-fold compression to $\Delta t_{\text{opt}} = 121$ fs (FWHM) at $N_{\text{eff}} = 2.0$. The compression occurred after around 15 cm propagation, so spatial walk-off would be an issue here. Increasing the soliton order to $N_{\text{eff}} = 2.6$ the pulse becomes more distorted, but still compresses to around 150 fs FWHM after 9.5 cm, a more realistic interaction length. Finally, at $N_{\text{eff}} = 3.0$ the pulse becomes too distorted as the GVM effects become stronger.

In the two cases the pulses therefore eventually compress to the same duration, which is the limit imposed by the nonlocal GVM effects. The more energetic pulses in case (2) allow for a more defocused pump beam so the compression should be less affected by diffraction. On the other hand, as the pulses are longer they compress later, so spatial walk-off is a more severe issue. A more optimal situation in both cases would therefore be more energetic pulses so the pump can be defocused with a factor 2-3. This would diminish spatial walk-off effects.

IV. CONCLUSION

Here we have shown that lithium niobate (LN) crystals in a type I cascaded SHG interaction can provide moderate compression of fs pulses from Yb-based fiber amplifier systems (1.03 μm wavelength). The phase mismatch was controlled through angle tuning (critical phase matching interaction). Using numerical simulations we found that the best compression was to around 120 fs FWHM after around 10 cm propagation.

Better compression was prevented in part by strong GVM effects, caused by strong dispersion in the LN crystal, and competing material Kerr nonlinear effects. These are focusing of nature and counteract the defocusing Kerr-like nonlinearities from the cascaded SHG. In order to make the total nonlinear phase shift negative

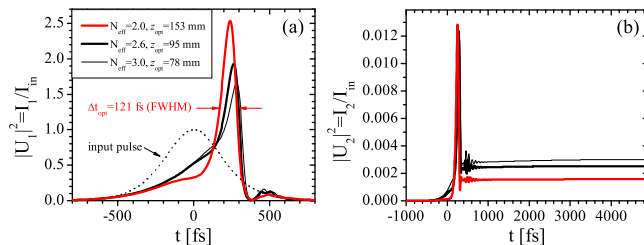


FIG. 8. (Color online) Numerical simulations using 450 fs 50 μJ input pulses and taking $\Delta k = 45$ mm⁻¹. The best pulse was observed for $N_{\text{eff}} = 2.0$ (red curve) where pulse compression occurs after 15 cm. The black curves show what happens as the effective soliton order increases (in which case the optimal compression point occurs sooner).

the phase mismatch had to be taken quite low, and in this regime GVM effects dominate (the “nonstationary” regime). GVM imposes a strongly nonlocal temporal response in the cascaded nonlinearity that feeds most of the converted energy into a narrow red-shifted peak. In the temporal trace this gave a SH with a multi-ps long trailing component. The FW therefore experienced a distorted compression less the soliton order was kept very low. For such low soliton orders the compression distance increases substantially, but here the strong dispersion of the LN crystal actually becomes an advantage: due to a large GVD the soliton dynamics occur in much shorter crystals than usual, and the numerics indicated compression in realistic crystal lengths (10 cm).

It was noted that using low soliton orders gave a compressed pulse retaining most of the input pulse energy (in the cases we showed around 80%), and that the unavoidable soliton pedestal was less pronounced.

We also discussed the implications of using long crystals. Spatial walk-off will be an issue since it is a critical phase matching scheme is used that exploits birefringence, and also diffraction can be a problem. In order to counteract these detrimental effects the pump pulses need to be as energetic and short as possible. Two cases were highlighted taken from commercially available systems, and we argued that diffraction should not prevent observing the predicted compression, but that some sort of walk-off compensation might be needed. Future systems with more energetic pulses and reasonably short pulse durations (< 500 fs) would be able to beat the walk-off problem. Walk-off could also be prevented by using a noncritical type I phase matching scheme ($\theta = \pi/2$) and increasing the temperature slightly to around 45° C.

We finally noted that the peculiar SH shape in the nonstationary regime gave a very characteristic spectrogram: as mentioned above nonlocal GVM effects resulted in a sharp spectral red-shifted peak with a long multi-ps trailing temporal component. Another pulse component was instead locked to the group velocity of the compressed FW soliton. This locked visible pulse was located at the SH wavelength (515 nm), quite far from the red-shifted peak. We showed that a simple bandpass filter could actually remove the detrimental red-shifted peak leaving a very clean 80 fs visible pulse ($\lambda = 515$ nm). This is the opposite approach compared to other studies, see e.g. [23, 25], where focus was on exploiting “spectral compression” of fs pulses to obtain longer ps pulses. Despite that the cascaded SHG by nature has a low conversion efficiency, the pulse energy of this short visible pulse can easily be 50-100 nJ. Such pulses could be used for two-color ultra-fast energetic pump-probe spectroscopy.

This study showed that cascaded quadratic pulse compression is possible even in a very dispersive nonlinear crystal. However, if compression occurs in a medium with stronger quadratic nonlinearities then it would be possible to increase the phase mismatch, and thereby enter the stationary regime where the nonlocal GVM effects are much weaker. The benefit would be triple: cleaner

compressed pulses could be generated, higher soliton orders could be used to achieve stronger compression, and it would occur in a shorter crystal. This conclusion is in line with what was noted previously in a fiber context [26], where one of us found that the very dispersive nature of wave-guided cascaded SHG could be overcome if a strong enough quadratic nonlinearity is present. We are currently investigating other possible nonlinear crystals and phase matching conditions to achieve this.

V. ACKNOWLEDGMENTS

Support is acknowledged from the Danish Council for Independent Research (Technology and Production Sciences, grant no. 274-08-0479 *Femto-VINIR*, and Natural Sciences, grant no. 21-04-0506). Jeff Moses and Binbin Zhou are acknowledged for useful discussions.

Appendix A: LN crystal parameters

LN is a negative uniaxial crystal of symmetry class $3m$. Its low damage threshold due to photorefractive effects and problems with green induced IR absorption can be improved dramatically by doping the crystal, in particular with MgO doping [27, 28]. 1% MgO doping in stoichiometric LN (1% MgO:sLN) is enough to practically remove photorefractive effects and increase dramatically the damage threshold, while 5% is needed in congruent LN (5% MgO:cLN) to do the same [28]. 1% MgO:sLN also has a shorter UV absorption edge ($\lambda = 0.31 \mu\text{m}$).

We here use 1% MgO:sLN, and the Sellmeier equations from [22]: note that for 1% MgO:sLN they only measured n_e , but we checked that the 5% MgO:cLN n_o Sellmeier equation matches well (at room temperature) the 1% sLN n_o equation from [29]. The quadratic nonlinear coefficients have been measured at $\lambda = 1.06 \mu\text{m}$ and are $d_{31} = -4.7$ pm/V and $d_{33} = 23.8$ pm/V [30], while $d_{22} = 2.1$ pm/V [31] was measured for undoped LN. The fact that $d_{31}d_{22} < 0$ has been established in, e.g., [32]. The effective quadratic nonlinearity of the type I $oo \rightarrow e$ interaction is given by Eq. (4). Because $d_{31}d_{22} < 0$ [32] the maximum nonlinearity is realized with $\phi = -\pi/2$.

Appendix B: Anisotropic Kerr nonlinear refraction

We previously studied type I cascaded SHG in a BBO crystal [16–18], assuming an isotropic Kerr nonlinearity

$$\chi_{\text{eff},11}^{(3)} = \chi_{\text{eff},22}^{(3)} = 3\chi_{\text{eff},12}^{(3)} \quad (\text{B1})$$

where $\chi_{\text{eff},jj}^{(3)}$ are the FW and SH SPM coefficients, and $\chi_{\text{eff},12}^{(3)}$ is the XPM coefficient. However, all quadratic nonlinear crystals are anisotropic, and below we address this.

Note first that the error made in assuming an isotropic response for the CQSC is probably small as the crucial

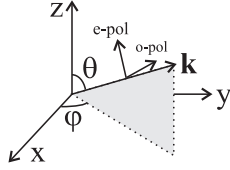


FIG. 9. Definition (in accordance with the IRE/IEEE standard [33]) of the crystal coordinate system xyz relative to the beam propagation direction indicated by \mathbf{k} .

parameter is the FW SPM coefficient. As we will see now for type I this is identical in the isotropic and in the anisotropic cases. However, it should be emphasized that the various experimental attempts to measure the Kerr nonlinear refractive index of nonlinear crystals do not always measure the tensor component relevant to our purpose, namely the c_{11} component, see Table I later. The analysis presented here should help understanding what exactly has been measured, and put the results into the context of cascaded quadratic soliton compression.

For a nonlinear crystal in the symmetry group $3m$ (LN and BBO) there are 37 nonzero elements for the $\underline{\underline{\chi}}^{(3)}$ tensor, and of these only 14 are independent [34]

$$\begin{aligned}
xxxx &= yyyy = xxyy + xyxy + xyxy \\
xxzz &= xzxx = xzzx = yyzz = yzyz = yzzy \\
&= zyyz = zyzy = zzyy = zxxx = zxxz = zzzx \\
xxyy &= xyxy = xyxy = yxxy = yxyx = yxyx \\
xxyz &= xxzy = xyxz = xyzx = xzxy = xzyx \\
&= -yyyz = -yyzy = -yzyy = yxxz = yxxz \\
&= yzxx = -zyyy = zxyy = zxyx = zyxx \\
zzzz &
\end{aligned} \tag{B2}$$

where Kleinman symmetry has been invoked, and the polarization relative to the crystal coordinate system is defined in Fig. 9. Under Kleinman symmetry the nonlinear coefficients are assumed dispersionless and the criterion for this assumption is that the system is far from any resonances. Using the notation $\chi_{ijkl}^{(3)} = c_{\mu m}$ where

$$\begin{aligned}
\text{for } \mu : & \quad x \rightarrow 1 \quad y \rightarrow 2 \quad z \rightarrow 3 \\
\text{for } m : & \quad xxx \rightarrow 1 \quad yyy \rightarrow 2 \quad zzz \rightarrow 3 \quad yyz \rightarrow 4 \\
& \quad yyz \rightarrow 5 \quad xzz \rightarrow 6 \quad xzx \rightarrow 7 \quad xyy \rightarrow 8 \\
& \quad xxy \rightarrow 9 \quad xyz \rightarrow 0
\end{aligned} \tag{B3}$$

these tensor components are equivalent to

$$\begin{aligned}
c_{11} &= c_{22} = 3c_{18} \\
c_{16} &= c_{24} = c_{35} = c_{37} \\
c_{18} &= c_{29} \\
c_{10} &= -c_{25} = c_{27} = -c_{32} = c_{39} \\
c_{33} &
\end{aligned} \tag{B4}$$

On the reduced form the cubic tensor becomes

$$\underline{\underline{\underline{\chi}}} = \begin{bmatrix} c_{11} & 0 & 0 & 0 & 0 & c_{16} & 0 & \frac{c_{11}}{3} & 0 & c_{10} \\ 0 & c_{11} & 0 & c_{16} & -c_{10} & 0 & c_{10} & 0 & \frac{c_{11}}{3} & 0 \\ 0 & -c_{10} & c_{33} & 0 & c_{16} & 0 & c_{16} & 0 & c_{10} & 0 \end{bmatrix} \tag{B5}$$

These results conform with the IRE/IEEE standard [35].

We now want to evaluate the cubic nonlinear response for a type I interaction. Using the notation from [17] the cubic nonlinear polarization response is

$$\mathbf{P}_{\text{NL}}^{(3)} = \varepsilon_0 \underline{\underline{\underline{\chi}}}^{(3)} : \mathbf{E} \mathbf{E} \mathbf{E} \tag{B6}$$

We have here only considered an instantaneous (electronic) cubic nonlinear response [36]. Let us consider the type I SHG interaction where two ordinarily polarized FW photons are converted to an extraordinarily polarized SH photon ($oo \rightarrow e$). In the coordinate system according to the IRE/IEEE standard [33], see Fig. 9, the unit vectors for o -polarized and e -polarized light are

$$\mathbf{e}^o = \begin{bmatrix} -\sin \phi \\ \cos \phi \\ 0 \end{bmatrix} \quad \mathbf{e}^e = \begin{bmatrix} -\cos \theta \cos \phi \\ -\cos \theta \sin \phi \\ \sin \theta \end{bmatrix} \tag{B7}$$

where walk-off has been neglected.

We then introduce slowly varying envelopes polarized along arbitrary directions

$$\mathbf{E}(t) = \text{Re}[\mathbf{u}_1 \mathcal{E}_1(t) e^{-i\omega_1 t} + \mathbf{u}_2 \mathcal{E}_2(t) e^{-i\omega_2 t}] \tag{B8}$$

where \mathbf{u}_j is the unit polarization vector. For type I SHG we have $\mathbf{u}_1 = \mathbf{e}^o$ and $\mathbf{u}_2 = \mathbf{e}^e$. The nonlinear slowly varying polarization response

$$\mathbf{P}_{\text{NL}}^{(3)}(t) = \text{Re}[\mathbf{u}_1 P_{\text{NL},1}^{(3)}(t) e^{-i\omega_1 t} + \mathbf{u}_2 P_{\text{NL},2}^{(3)}(t) e^{-i\omega_2 t}]$$

then becomes

$$P_{\text{NL},i}^{(3)} = \frac{3}{4} \varepsilon_0 \left[\chi_{\text{eff},ii}^{(3)} |\mathcal{E}_i|^2 + 2\chi_{\text{eff},ij}^{(3)} |\mathcal{E}_j|^2 \right] \mathcal{E}_i, \tag{B9}$$

where $i, j = 1, 2$ and $j \neq i$. We have here only included phase-matched components and frequency-mixing terms where $2\omega_1 - \omega_2 = 0$. The numerical prefactor $\frac{3}{4}$ is the K -factor [37] for a third order nonlinear effect creating an intensity dependent refractive index with degenerate frequencies, and the factor 2 on the XPM terms $\chi_{\text{eff},ij}^{(3)}$ stems from the fact that the K -factor for cross-phase modulation with non-degenerate frequencies is $\frac{3}{2}$.

For calculating the cubic nonlinear coefficients, it is convenient to use an effective cubic nonlinearity [38]

$$\chi_{\text{eff}}^{(3)} = \mathbf{u}_d \cdot \underline{\underline{\underline{\chi}}}^{(3)} : \mathbf{u}_a \mathbf{u}_b \mathbf{u}_c = \mathbf{u}_d \cdot \underline{\underline{\underline{\mathcal{E}}}} \cdot \mathbf{u}^{(3)}, \tag{B10}$$

$a, b, c, d = 1, 2$. Here \mathbf{u}_d is the unit vector of the field under consideration; thus, if we are interested in calculating the cubic nonlinear polarization for the FW [taking $i = 1$ in Eq. (B9)], then $\mathbf{u}_d = \mathbf{u}_1$. The other three unit vectors $\mathbf{u}_{a,b,c}$ are the unit vectors of each field appearing in

Eq. (B6), and can in the case we are considering here be either \mathbf{u}_1 or \mathbf{u}_2 according to the identity (B8). Most combinations are not phase matched or have $2\omega_1 - \omega_2 \neq 0$, and are therefore not included in Eq. (B9). The rank 4 tensor on reduced form, as given by Eq. (B5) for LN, can be used to find the tensor product $\underline{\chi}^{(3)}:\mathbf{u}_a\mathbf{u}_b\mathbf{u}_c$ as a simple matrix-vector product $\underline{\underline{c}} \cdot \mathbf{u}^{(3)}$ where

$$\mathbf{u}^{(3)} = \begin{bmatrix} L_{xxx} \\ L_{yyy} \\ L_{zzz} \\ L_{yzz} + L_{zyz} + L_{zzy} \\ L_{yyz} + L_{yzy} + L_{zyy} \\ L_{xzz} + L_{zxx} + L_{zzx} \\ L_{xxz} + L_{xzx} + L_{zxx} \\ L_{xyy} + L_{yxy} + L_{yyx} \\ L_{xxy} + L_{xyx} + L_{yxx} \\ L_{xyz} + L_{xzy} + L_{zxy} + L_{yxz} + L_{zyx} + L_{zyx} \end{bmatrix} \quad (\text{B11})$$

Here $L_{jkl} \equiv u_{a,j}u_{b,k}u_{c,l}$ where the $ijkl$ indices refer to the x, y or z components of the unit vectors.

It is convenient at this stage to simplify the notation based on the type I SHG interaction we are interested in. The effective cubic nonlinearity (B10) then reduces to the nonlinear coefficients appearing in Eq. (B9)

$$\chi_{\text{eff},ij}^{(3)} = \mathbf{u}_i \cdot \underline{\underline{\chi}}^{(3)}:\mathbf{u}_i\mathbf{u}_j\mathbf{u}_j \quad (\text{B12})$$

The SPM terms can now be calculated as follows. The FW SPM interaction has $i = j = 1$ in Eq. (B12), and is an $ooo \rightarrow o$ process: $\mathbf{u}_1 = \mathbf{e}^o$. The SH SPM interaction has $i = j = 2$ and is an $eee \rightarrow e$ process, so $\mathbf{u}_2 = \mathbf{e}^e$.

We then need to calculate $\underline{\underline{\chi}}^{(3)}:\mathbf{u}_i\mathbf{u}_i\mathbf{u}_i$ using the reduced notation. Since for the SPM terms all the unit vectors in $\mathbf{u}^{(3)}$ are degenerate in frequency, all L_{jkl} components in a given vector entry are identical, e.g. $L_{yzz} = L_{zyz} = L_{zzy}$. We then get for the FW

$$\underline{\underline{\chi}}^{(3)}:\mathbf{u}_1\mathbf{u}_1\mathbf{u}_1 = \begin{bmatrix} -c_{11} \sin \phi \\ c_{11} \cos \phi \\ -c_{10} \cos^3 \phi \end{bmatrix} \quad (\text{B13})$$

A similar expression can be calculated for the SH SPM component, although it is substantially more complex. In the final step we carry out the vector dot product of these vectors with \mathbf{u}_i , as dictated by Eq. (B12), and get for the FW ($i = 1$) and the SH ($i = 2$) [35]

$$\chi_{\text{eff},11}^{(3)} = c_{11} \quad (\text{B14})$$

$$\chi_{\text{eff},22}^{(3)} = -4c_{10} \sin \theta \cos^3 \theta \sin 3\phi + c_{11} \cos^4 \theta + \frac{3}{2}c_{16} \sin^2 2\theta + c_{33} \sin^4 \theta \quad (\text{B15})$$

For the XPM terms note that the three unit vectors used to calculate Eq. (B11) are non-degenerate in frequency. As an example, for $\underline{\underline{\chi}}^{(3)}:\mathbf{u}_2\mathbf{u}_1\mathbf{u}_1$ terms like

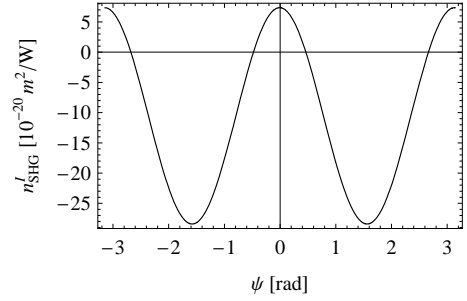


FIG. 10. The calculated effective Kerr nonlinear contributions from cascaded SHG to the measured Kerr nonlinear refractive index by Kulagin et al. [39]. The beam propagates with $\theta = \pi/2$ into a LN crystal, and ψ denotes the polarization angle ($\psi = 0$ gives o -polarized light, while $\psi = \pi/2$ gives e -polarized light). The angle ϕ was not reported, but we checked it has little influence on the n_{SHG}^I value shown here.

$L_{xyy} + L_{yxy} + L_{yyx}$ must be evaluated, whose components are $L_{xyy} = -\cos \theta \cos^3 \phi$ and $L_{yxy} = L_{yyx} = \cos \theta \sin^2 \phi \cos \phi$. This gives $\chi_{\text{eff},12}^{(3)} = \chi_{\text{eff},21}^{(3)}$ and [35, 39]

$$\chi_{\text{eff},12}^{(3)} = \frac{1}{3}c_{11} \cos^2 \theta + c_{16} \sin^2 \theta + c_{10} \sin 2\theta \sin 3\phi \quad (\text{B16})$$

The next step is to obtain the the values for LN of each component in Eqs. (B14)-(B16). The value of the cubic nonlinear refractive index has been measured by many authors and for many different pulse durations and crystal cuts. In Tab. I the $\chi^{(3)}$ tensor components and the n_{Kerr}^I are reported in electrostatic units values, and the latter is also given in SI units (see App. C for details).

In one of the earliest studies the tensorial nature of LN was studied [44]. Another early study found that $c_{11} = 3c_{10}$ [48]. Later studies used Z-scan methods and often a nonlinear refractive index value was found without any mentioning of the tensorial nature of the cubic nonlinear susceptibility. The cascaded quadratic contributions were also often forgotten or neglected.

A recent study by Kulagin et al. went into a detailed experimental determination of the various cubic tensor components of LN, and found $c_{11} = 2.4 \times 10^{-13}$ esu at $\lambda = 1.06 \mu\text{m}$, and that $c_{18} = 1.2c_{16} = 1.4c_{33}$ [39]. Through the relation $c_{11} = 3c_{18}$, see Eq. (B4), the other coefficients are $c_{16} = c_{11}/3.6$, $c_{33} = c_{11}/4.2$. A problem with this study is that the cascaded quadratic nonlinear contributions to the observed Z-scan results were neglected. Instead, based on an analysis of the anisotropic Kerr tensor components the Z-scan transmission function was calculated, and the various tensor components were found by fitting to experimental data. In the experiment the pump propagated with $\theta = \pi/2$, i.e. with the \mathbf{k} -vector perpendicular to the OA. The angle of the polarization vector was then varied; this gives either pure o -polarized light, pure e -polarized light, or a linear mixture.

We have done an analysis of the various cascaded SHG processes that come into play ($oo \rightarrow o$, $oo \rightarrow e$, $oe \rightarrow e$, $oe \rightarrow o$, $ee \rightarrow e$, and $ee \rightarrow o$), evaluated their respective

λ [nm]	$\chi_{\text{eff}}^{(3)}$ [10^{-13} esu]	n_{Kerr}^I [10^{-13} esu]	n_{Kerr}^I [10^{-20} m ² /W]	t_{FWHM} [ps]	Rep.	θ [deg]	pol	n	c_{ij}	Ref.	Note
1064	1.1	<u>4.8</u>	9.1	30	single	90	<i>e</i>	2.2	c_{33}	[40]	<i>x</i> -cut
1064	0.73	<u>3.2</u>	6.0	55	2 Hz	90	<i>o</i>	2.2337 ^a	c_{11}	[41]	paraxial fit
1064	0.66	<u>2.9</u>	5.4	55	2 Hz	90	<i>o</i>	2.2337 ^a	c_{11}	[41]	Gaussian fit
1064	<u>2.4</u>	10	19	55	2 Hz	90	<i>o</i>	2.2337	c_{11}	[39]	Fit to transmission curve
1064	0.80	3.4	6.3	55	2 Hz	90	<i>e+o</i>	2.2337	c_{12}, c_{18}	[39]	" , $c_{12} = c_{11}/3$
1064	0.57	2.8	4.9	55	2 Hz	90	<i>e</i>	2.1495	c_{33}	[39]	" , $c_{33} = c_{12}/1.4$
1064	0.67	2.9	5.5	55	2 Hz	90	<i>e+o</i>	2.1912	c_{23}, c_{16}	[39]	" , $c_{23} = c_{12}/1.2$
800	1.8	7.8	<u>15</u>	0.42	1 kHz	?	?	2.1677 ^a	?	[42]	<i>x</i> -cut, <i>z</i> -cut
780	2.6	11.0	<u>20</u>	0.15	76 MHz	0	<i>o</i>	2.2552 ^a	c_{11}	[43]	6% MgO:LN, <i>z</i> -cut
577	<u>1.6</u>	6.6	12	5,000	40 Hz	0	<i>o</i>	2.301 ^a	c_{18}	[44]	$c_{18} = c_{11}/3$
532	10	<u>44</u>	83	22	single	90	<i>e</i>	2.23	c_{33}	[40]	<i>x</i> -cut
532	6.6	28	<u>53</u>	25	10 Hz	0	<i>o</i>	2.2244 ^a	c_{11}	[45]	<i>z</i> -cut
520	<u>5.0</u>	21	39	0.2	1 kHz	90	<i>e</i>	2.24	c_{33}	[46]	5% MgO 0.06% Fe cLN

^a Linear refractive index not provided; this value was calculated by us for conversion purposes.

TABLE I. Nonlinear Kerr refractive index of LN measured mainly by the Z-scan method [47]. The underlined results are the values reported. The other entries have been calculated using Eqs. (C8)-(C11).

d_{eff} -values and phase mismatch values as the input polarization angle changes. In total we arrived at a strongly varying cascaded contribution shown in Fig. 10. At $\psi = 0$ the contribution from n_{SHG}^I is focusing, implying that the c_{11} component in Kulagin et al. might be too high with a factor of 7.0×10^{-20} m²/W. There are also strongly defocusing contributions at other polarization angles, which should give rise to an underestimated value of the other tensor components. Moreover, the overall shape reminds strongly of the shape found in Fig. 5 in [39]: the focusing peaks from cascaded SHG could explain the valleys found there, and the defocusing valleys from cascaded SHG could instead explain the peaks. In summary we believe the c_{11} value to be too high, and the relation to the other tensor components to be dubious.

There are other issues with the Z-scan method: If the repetition rate is too high, there will also be contributions to the measured n_{Kerr}^I from thermal effects as well as two-photon excited free carriers [49], and hence n_{Kerr}^I does not contain just the instantaneous electronic response, as it is supposed to. Similarly conclusions can be made for pulses longer than 1 ps. For more on these issues, see e.g. [50].

For the CQSC system the by far most important component is the FW SPM coefficient $n_{\text{Kerr},11}^I$. The SH SPM and the XPM coefficients only play minor roles in extreme cases close to transitions (e.g., close to the soliton existence line in Fig. 3). We checked in the cases we studied in this paper that even increasing the SH SPM and XPM Kerr coefficient several times the isotropic values did not significantly change the compression results.

Therefore until detailed reliable measurements of the cubic tensorial components of LN become available, we decided to use an isotropic Kerr response, and focus on using a realistic value of the FW SPM coefficient. The best choice seems to be $n_{\text{Kerr}}^I = 20 \times 10^{-20}$ m²/W at $\lambda = 0.78 \mu\text{m}$ found in Ref. [43]. In this experiment they have $\theta = 0$ and thus what they measure is $\chi_{\text{eff}}^{(3)} = c_{11}$. For orthogonal input polarization (corresponding to $\phi =$

$0, \pi/2$, both cases *o*-polarized) they find the same value as they should since this $\chi_{\text{eff}}^{(3)}$ does not depend on ϕ , cf. Eq. (B14). Since they used fs pulses problems with long pulses are avoided. The high repetition rate could cause concern, but they checked that lowering it to below 1 MHz did not change the results. Finally, the contribution from the cascaded nonlinearities should be low: we estimate $|n_{\text{SHG}}^I| < 10^{-21}$ m²/W.

As discussed later in App. D we use Miller's rule to convert the nonlinear coefficients to the $\lambda_1 = 1.03 \mu\text{m}$ that we use in the simulations in Sec. III. This implies that in the numerics we use $n_{\text{Kerr},11}^I = 18.0 \times 10^{-20}$ m²/W, $n_{\text{Kerr},12}^I = 6.0 \times 10^{-20}$ m²/W, and $n_{\text{Kerr},22}^I = 18.3 \times 10^{-20}$ m²/W.

Appendix C: Conversion relations

Often the nonlinear susceptibility is reported in Gaussian cgs units (esu) instead of the SI mks units. The conversion between esu and SI is

$$\chi_{\text{SI}}^{(3)} = 4\pi\chi_{\text{esu}}^{(3)}(10^4/c)^2 \quad (\text{C1})$$

where c is the speed of light in SI units. The 4π comes from the Gaussian unit definition of the electric displacement $\mathbf{D} = \mathbf{E} + 4\pi\mathbf{P}$, and the $10^4/c$ comes from converting statvolt/cm to V/m.

In most cases the nonlinear Kerr refractive index is used. It is usually defined as the intensity-dependent change Δn in the refractive index observed by the light

$$n = n_0 + \frac{1}{2}\Delta n = n_0 + n_{\text{Kerr}}\frac{1}{2}|\mathcal{E}_0|^2 = n_0 + n_{\text{Kerr}}^I I \quad (\text{C2})$$

Here n_0 represents the linear refractive index, \mathcal{E}_0 and I_0 the input electric field and intensity, respectively. In our case the total polarization (linear and cubic, in absence of quadratic nonlinearities) can be written as $P_i = P_i^{(1)} + P_{\text{NL},i}^{(3)} = \varepsilon_0(\varepsilon_i + \varepsilon_{\text{NL},i})\mathcal{E}_i$. Now writing the sum of the

linear and nonlinear relative permittivities as $\varepsilon_i + \varepsilon_{\text{NL},i} = (n_i + \frac{1}{2}\Delta n_i)^2 \simeq n_i^2 + n_i\Delta n_i$ (here we take $\Delta n_i \ll n_i$) then we can write the change in refractive index due to the Kerr nonlinearity on the form

$$\Delta n_i \simeq n_{\text{Kerr},ii}|\mathcal{E}_i|^2 + 2n_{\text{Kerr},ij}|\mathcal{E}_j|^2 \quad (\text{C3})$$

When comparing with Eq. (B9) we get in SI units [51]

$$n_{\text{Kerr},ij}(\text{SI}) = \frac{3}{4n_i}\chi_{\text{eff},ij}^{(3)}(\text{SI}), \quad i, j = 1, 2 \quad (\text{C4})$$

Note that the numerical prefactor 3/4 is the K -factor discussed above. Adopting the intensity notation the change in refractive index is $\Delta n_i \simeq 2(n_{\text{Kerr},ii}^I I_i + 2n_{\text{Kerr},ij}^I I_j)$, and since in SI units $I_i = \frac{1}{2}\varepsilon_0 n_i c |\mathcal{E}_i|^2$, we get

$$n_{\text{Kerr},ij}^I(\text{SI}) = \frac{1}{n_j \varepsilon_0 c} n_{\text{Kerr},ij}(\text{SI}) \quad (\text{C5})$$

$$= \frac{3}{4n_i n_j \varepsilon_0 c} \chi_{\text{eff},ij}^{(3)}(\text{SI}) \quad (\text{C6})$$

With Gaussian cgs units we would instead get [51]

$$n_{\text{Kerr},ij}(\text{esu}) = \frac{3\pi}{n_i} \chi_{\text{eff},ij}^{(3)}(\text{esu}) \quad (\text{C7})$$

$$n_{\text{Kerr},ij}^I(\text{esu}) = \frac{4\pi}{n_j c} n_{\text{Kerr},ij}(\text{esu}) \quad (\text{C8})$$

$$= \frac{12\pi^2}{n_i n_j c} \chi_{\text{eff},ij}^{(3)}(\text{esu}) \quad (\text{C9})$$

We have here used that in Gaussian units the intensity is $I_i(\text{esu}) = (8\pi)^{-1} n_i c |\mathcal{E}_i(\text{esu})|^2$. The K -factor appears also in Eq. (C7) as $\frac{3}{4}4\pi = 3\pi$. Note that c is still in SI units in these expressions.

The connection between the Gaussian and SI systems can best be done via Eq. (C1) and (C6) to give [37, 51]

$$\chi_{\text{eff},ij}^{(3)}(\text{esu}) = \frac{n_i n_j c}{120\pi^2} n_{\text{Kerr},ij}^I(\text{SI}) \quad (\text{C10})$$

$$n_{\text{Kerr},ij}(\text{esu}) = \frac{n_j c}{40\pi} n_{\text{Kerr},ij}^I(\text{SI}) \quad (\text{C11})$$

where we have used that the SI system defines $\varepsilon_0 c^2 = 1/\mu_0 = 10^7/4\pi$ using $c = 299\,792\,458$ m/s exactly.

Note that often the definition of the Kerr nonlinear refractive index is $n = n_0 + \Delta n = n_0 + n_{\text{Kerr}}|\mathcal{E}|^2 = n_0 + n_{\text{Kerr}}^I I$ (in Ref. [17] we used this notation), which introduces an additional factor of 2 between n_{Kerr} and n_{Kerr}^I , while the relation between n_{Kerr}^I and $\chi^{(3)}$ is unaffected. Thus, working with $\chi^{(3)}$ and n_{Kerr}^I is the safest because one never has to worry about this factor of 2; as an example Eq. (C10) is still valid, while with the alternative definition Eq. (C11) becomes $n_{\text{Kerr}}(\text{esu}) = (n_0 c/80\pi)n_{\text{Kerr}}^I(\text{SI})$ [37].

Appendix D: Wavelength scaling of the nonlinear susceptibility: Miller's delta

In the results presented here we account for the wavelength dependence of the nonlinear coefficients by using Miller's rule, which states that the following coefficients (the Miller's delta) are frequency independent [52]

$$\delta^{(2)} = \frac{\chi_{ijk}^{(2)}}{\chi_{ii}^{(1)} \chi_{jj}^{(1)} \chi_{kk}^{(1)}}, \quad i, j, k = x, y, z \quad (\text{D1})$$

and we remind that the linear susceptibility is $1 + \chi_{ii}^{(1)} = n_i^2$. A similar relation holds for the cubic nonlinearity

$$\delta^{(3)} = \frac{\chi_{ijkl}^{(3)}}{\chi_{ii}^{(1)} \chi_{jj}^{(1)} \chi_{kk}^{(1)} \chi_{ll}^{(1)}}, \quad i, j, k, l = x, y, z \quad (\text{D2})$$

We remark that Miller's delta is based on an anharmonic oscillator with a single resonant frequency and only gives a ballpark estimate of the value, and thus is not to be expected to have a large accuracy (see, e.g., [53, 54]). However, it has been shown to work decently for most nonlinear crystals [55].

-
- [1] M. Fermann and I. Hartl, IEEE J. Sel. Top. Quantum Electron. **15**, 191 (2009).
 - [2] J. Limpert, F. Röser, T. Schreiber, and A. Tünnermann, IEEE J. Sel. Top. Quantum Electron. **12**, 233 (2006).
 - [3] L. Kuznetsova and F. W. Wise, Opt. Lett. **32**, 2671 (2007).
 - [4] T. Eidam, F. Röser, O. Schmidt, J. Limpert, and A. Tünnermann, Appl. Phys. B **92**, 9 (2008).
 - [5] M. Nisoli, S. D. Silvestri, and O. Svelto, Appl. Phys. Lett. **68**, 2793 (1996); C. Hauri, W. Kornelis, F. Helbing, A. Heinrich, A. Couairon, A. Mysyrowicz, J. Biegert, and U. Keller, Appl. Phys. B **79**, 673 (2004).
 - [6] J. Chen, A. Suda, E. J. Takahashi, M. Nurhuda, and K. Midorikawa, Opt. Lett. **33**, 2992 (2008).
 - [7] L. F. Mollenauer, R. H. Stolen, and J. P. Gordon, Phys. Rev. Lett. **45**, 1095 (Sep 1980).
 - [8] D. Ouzounov, C. Hensley, A. Gaeta, N. Venkateraman, M. Gallagher, and K. Koch, Opt. Express **13**, 6153 (2005); J. Lægsgaard and P. J. Roberts, J. Opt. Soc. Am. B **26**, 783 (2009).
 - [9] X. Liu, L. Qian, and F. W. Wise, Opt. Lett. **24**, 1777 (1999).
 - [10] S. Ashihara, J. Nishina, T. Shimura, and K. Kuroda, J. Opt. Soc. Am. B **19**, 2505 (2002).
 - [11] F. W. Wise and J. Moses, "Self-focusing and self-defocusing of femtosecond pulses with cascaded quadratic nonlinearities," in *Self-focusing: Past and Present*, Topics in Applied Physics, Vol. 114, edited by R. W. Boyd, S. G. Lukishova, and Y. R. Shen (Springer, Berlin, 2009) pp. 481–506.
 - [12] J. Moses, E. Alhammali, J. M. Eichenholz, and F. W. Wise, Opt. Lett. **32**, 2469 (2007).

- [13] R. DeSalvo, D. Hagan, M. Sheik-Bahae, G. Stegeman, E. W. Van Stryland, and H. Vanherzeele, *Opt. Lett.* **17**, 28 (1992).
- [14] G. I. Stegeman, D. J. Hagan, and L. Torner, *Opt. Quantum Electron.* **28**, 1691 (1996).
- [15] J. Moses and F. W. Wise, *Opt. Lett.* **31**, 1881 (2006).
- [16] M. Bache, O. Bang, J. Moses, and F. W. Wise, *Opt. Lett.* **32**, 2490 (2007).
- [17] M. Bache, J. Moses, and F. W. Wise, *J. Opt. Soc. Am. B* **24**, 2752 (2007).
- [18] M. Bache, O. Bang, W. Krolikowski, J. Moses, and F. W. Wise, *Opt. Express* **16**, 3273 (2008).
- [19] S. Ashihara, T. Shimura, K. Kuroda, N. E. Yu, S. Kurimura, K. Kitamura, M. Cha, and T. Taira, *Appl. Phys. Lett.* **84**, 1055 (2004); X. Zeng, S. Ashihara, N. Fujioka, T. Shimura, and K. Kuroda, *Opt. Express* **14**, 9358 (2006).
- [20] G. P. Agrawal, *Nonlinear fiber optics*, 3rd ed. (Academic Press, London, 2001).
- [21] J.-J. Zondy, M. Abed, and S. Khodja, *J. Opt. Soc. Am. B* **11**, 2368 (1994).
- [22] O. Gayer, Z. Sacks, E. Galun, and A. Arie, *Appl. Phys. B* **91**, 343 (2008).
- [23] L. D. Noordam, H. J. Bakker, M. P. de Boer, and H. B. van Linden van den Heuvell, *Opt. Lett.* **15**, 1464 (1990); H. J. Bakker, W. Joosen, and L. D. Noordam, *Phys. Rev. A* **45**, 5126 (1992); W. Su, L. Qian, H. Luo, X. Fu, H. Zhu, T. Wang, K. Beckwitt, Y. Chen, and F. Wise, *J. Opt. Soc. Am. B* **23**, 51 (2006).
- [24] S. Linden, H. Giessen, and J. Kuhl, *Phys. Stat. Sol. B* **206**, 119 (1998).
- [25] M. A. Marangoni, D. Brida, M. Quintavalle, G. Cirimi, F. M. Pigozzo, C. Manzoni, F. Baronio, A. D. Capobianco, and G. Cerullo, *Opt. Express* **15**, 8884 (2007).
- [26] M. Bache, *J. Opt. Soc. Am. B* **26**, 460 (2009).
- [27] D. A. Bryan, R. Gerson, and H. E. Tomaschke, *Appl. Phys. Lett.* **44**, 847 (1984); Y. Furukawa, K. Kitamura, S. Takekawa, A. Miyamoto, M. Terao, and N. Suda, *ibid.* **77**, 2494 (2000); Y. Furukawa, K. Kitamura, S. Takekawa, K. Niwa, and H. Hatano, *Opt. Lett.* **23**, 1892 (1998).
- [28] Y. Furukawa, K. Kitamura, A. Alexandrovski, R. K. Route, M. M. Fejer, and G. Foulon, *Appl. Phys. Lett.* **78**, 1970 (2001).
- [29] M. Nakamura, S. Higuchi, S. Takekawa, K. Terabe, Y. Furukawa, and K. Kitamura, *Jap. J. Appl. Phys.* **41**, L49 (2002).
- [30] I. Shoji, T. Ue, K. Hayase, A. Arai, M. Takeda, S. Nakajima, A. Neduka, R. Ito, and Y. Furukawa, in *Nonlinear Optics: Materials, Fundamentals and Applications* (Optical Society of America, 2007) p. WE30.
- [31] R. C. Miller, W. A. Nordland, and P. M. Bridenbaugh, *J. Appl. Phys.* **42**, 4145 (1971); V. Dmitriev, G. Gurzadyan, and D. Nikogosyan, *Handbook of Nonlinear Optical Crystals*, Springer Series in Optical Sciences, Vol. 64 (Springer, Berlin, 1999).
- [32] R. S. Klein, G. E. Kugel, A. Maillard, and K. Polgar, *Ferroelectrics* **296**, 57 (2003).
- [33] D. Roberts, *IEEE J. Quantum Electron.* **28**, 2057 (1992).
- [34] B. Boulanger and J. Zyss, "International tables for crystallography," (Springer, 2006) Chap. 1.7 Nonlinear optical properties, pp. 178–219.
- [35] P. S. Banks, M. D. Feit, and M. D. Perry, *J. Opt. Soc. Am. B* **19**, 102 (2002).
- [36] The Raman response of LN has been studied in the past, see, e.g., A. S. Barker and R. Loudon, *Phys. Rev.* **158**, 433 (1967), but since we deal with quite long pulses > 50 fs it is safe to neglect such effects in our simulations
- [37] P. N. Butcher and D. Cotter, *The elements of nonlinear optics* (Cambridge University Press, Cambridge, 1990).
- [38] X. L. Yang and S. W. Xie, *Appl. Opt.* **34**, 6130 (1995).
- [39] I. A. Kulagin, R. A. Ganeev, R. I. Tugushev, A. I. Rysanyansky, and T. Usmanov, *J. Opt. Soc. Am. B* **23**, 75 (2006).
- [40] R. DeSalvo, A. A. Said, D. Hagan, E. W. Van Stryland, and M. Sheik-Bahae, *IEEE J. Quantum Electron.* **32**, 1324 (1996).
- [41] R. Ganeev, I. Kulagin, A. Rysanyansky, R. Tugushev, and T. Usmanov, *Opt. Commun.* **229**, 403 (2004).
- [42] J. Burghoff, H. Hartung, S. Nolte, and A. Tünnermann, *Appl. Phys. A* **86**, 165 (2007).
- [43] H. P. Li, C. H. Kam, Y. L. Lam, and W. Ji, *Optical Materials* **15**, 237 (2001).
- [44] J. J. Wynne, *Phys. Rev. Lett.* **29**, 650 (1972).
- [45] H. Li, F. Zhou, X. Zhang, and W. Ji, *Opt. Commun.* **144**, 75 (1997).
- [46] Z. H. Wang, X. Z. Zhang, J. J. Xu, Q. A. Wu, H. J. Qiao, B. Q. Tang, R. Rupp, Y. F. Kong, S. L. Chen, Z. H. Huang, B. Li, S. G. Liu, and L. Zhang, *Chin. Phys. Lett.* **22**, 2831 (2005).
- [47] M. Sheik-Bahae, A. Said, T.-H. Wei, D. Hagan, and E. Van Stryland, *IEEE J. Quantum Electron.* **26**, 760 (Apr 1990).
- [48] H. J. Eichler, H. Fery, J. Knof, and J. Eichler, *Z. Physik B* **28**, 297 (1977).
- [49] T. D. Krauss and F. W. Wise, *Appl. Phys. Lett.* **65**, 1739 (1994).
- [50] A. Gnoli, L. Razzari, and M. Righini, *Opt. Express* **13**, 7976 (2005).
- [51] D. C. Hutchings, M. Sheik-Bahae, D. J. Hagan, and E. W. V. Stryland, *Opt. Quantum Electron.* **24**, 1 (1992).
- [52] R. C. Miller, *Appl. Phys. Lett.* **5**, 17 (1964).
- [53] M. I. Bell, *Phys. Rev. B* **6**, 516 (1972).
- [54] I. Shoji, T. Kondo, A. Kitamoto, M. Shirane, and R. Ito, *J. Opt. Soc. Am. B* **14**, 2268 (1997).
- [55] W. J. Alford and A. V. Smith, *J. Opt. Soc. Am. B* **18**, 524 (2001).